New Methodology Shows Short Atmospheric Lifetimes of Oxidized Sulfur and Nitrogen due to Dry Deposition

Katherine Hayden[1], Shao-Meng Li[1,2*], Paul Makar[1], John Liggio[1], Samar G. Moussa[1], Ayodeji Akingunola[1], Robert McLaren[3], Ralf M. Staebler[1], Andrea Darlington[1], Jason O'Brien[1], Junhua Zhang[1], Mengistu Wolde[4], Leiming Zhang[1]

[1]*Air Quality Research Division, Environment and Climate Change Canada, Toronto, Ontario, Canada, M3H 5T4*

[2]*College of Environmental Science and Engineering, Peking University, Beijing 100871 China*

[3]*Center for Atmospheric Chemistry, York University, 4700 Keele Street, Toronto, Ontario, Canada*

[4]*National Research Council Canada, Flight Research Laboratory, Ottawa, Canada K1A 0R6*

*corresponding authors shaomeng.li@pku.edu.cn; Katherine.hayden@canada.ca

For submission to *Atmospheric Chemistry and Physics*

Abstract

The atmospheric lifetimes of pollutants determine their impacts on human health, ecosystems and climate and yet, pollutant lifetimes due to dry deposition over large regions have not been determined from measurements. Here, a new methodology based on aircraft observations is used to determine the lifetimes of oxidized sulfur and nitrogen due to dry deposition over $(3-6) \times 10^3$ km^2 of boreal forest in Canada. Dry deposition fluxes decreased exponentially with distance from the Athabasca oil sands sources, located in northern Alberta, resulting in lifetimes of 2.2-26 hours. Fluxes were 2-14 and 1-18 times higher than model estimates for oxidized sulfur and nitrogen, respectively, indicating dry deposition velocities which were 1.2-5.4 times higher than those computed for models. A Monte-Carlo analysis with five commonly used inferential dry deposition algorithms indicates that such model underestimates of dry deposition velocity are typical. These findings indicate that deposition to vegetation surfaces are likely under-estimated in regional and global chemical transport models regardless of the model algorithm used. The model-observation gaps may be reduced if surface pH, and quasi-laminar and aerodynamic resistances in algorithms are optimized as shown in the Monte-Carlo analysis. Assessing the air quality and climate impacts of atmospheric pollutants on regional and global scales requires improved measurement-based understanding of atmospheric lifetimes of these pollutants.

1 Introduction

Deposition represents the terminating process for most air pollutants and the starting point for ecosystem impacts. Understanding deposition is critical in determining the atmospheric lifetimes and spatial scale of atmospheric transport of pollutants, which in turn, dictates their ecosystem (WHO, 2016; Solomon et al., 2007) and climate (Samset et al., 2014) impacts. In particular, atmospheric lifetimes (τ) of oxidized sulfur and nitrogen compounds influence their concentrations and column burdens in air, which affect air quality and hence human exposure (WHO, 2016). Furthermore, the lifetime of these species affects their contributions to atmospheric aerosols, with a consequent influence on climate via changes to radiative transfer through scattering and cloud formation (Solomon et al., 2007). In addition, their deposition can exceed critical load thresholds causing aquatic and terrestrial acidification, and eutrophication in the case of nitrogen deposition (Howarth, 2008; Bobbink et al., 2010; Doney, 2010; Vet et al., 2014; Wright et al., 2018). Quantifying τ and deposition thus provides a crucial assessment of these regional and global impacts.

Deposition occurs through wet and dry processes. While wet deposition fluxes can be measured directly (Vet et al., 2014), there are few validated methods for dry deposition fluxes (Wesley and Hicks, 2000), and none which estimates deposition over large regions. Dry deposition fluxes (F) may be obtained using micrometeorological measurements for pollutants for which fast response instruments are available. However, these results are only valid for the footprints of the observation sites, typically hundreds of meters (Aubinet e al., 2012), and their extrapolation to larger regions may suffer from representativeness issues. As a result, atmospheric lifetimes τ with respect to dry deposition have not been determined through direct observations. On a regional scale, dry deposition fluxes are typically derived using an inferential

56 approach by multiplying network-measured or model-predicted air concentrations with dry

57 deposition velocities (V_d) (Sickles and Shadwick, 2015; Fowler et al., 2009; Meyers et al., 1991),

58 which are derived using resistance-based inferential dry deposition algorithms (Wu et al., 2018),

59 and compared with limited micrometeorological flux measurements (Wesley and Hicks, 2000;

60 Wu et al., 2018; Finkelstein et al., 2000; Matsuda et al., 2006; Makar et al., 2018) for validation.

61 When applied to a regional scale, an inferential-algorithm derived V_d may have significant

62 uncertainties (Wesley and Hicks, 2000; Aubinet et al., 2012;Wu et al., 2018; Finkelstein et al.,

63 2000; Matsuda et al., 2006; Makar et al., 2018; Brook et al., 1997). For example, inferred V_d for

64 SO_2, despite being the most studied and best estimated, may be underestimated by 35% for forest

65 canopies (Finkelstein et al., 2000). Underestimated V_d for SO_2 and nitrogen oxides can

66 contribute to model over-prediction of regional and global SO_2 concentrations (Solomon et al.,

67 2007; Christian et al., 2015; Chin et al., 2000), or under-prediction of global oxidized nitrogen

68 dry deposition fluxes (Paulot et al., 2018; Dentener et al., 2006).

69   Here, a new approach is presented to determine τ with respect to dry deposition and F for

70 total oxidized sulfur (**TOS**, the sulfur mass in SO_2 and particle-SO_4 (pSO_4)) and total reactive

71 oxidized nitrogen (**TON**, the nitrogen mass in NO, NO_2, and others designated as NO_z) on a

72 spatial scale of $(3-6) \times 10^3$ km^2, using aircraft measurements. This approach provides a unique

73 methodology to determine τ and F over a large region. Coupled with analyses for chemical

74 reaction rates (for **TOS** compounds), the average V_d for **TOS** and **TON** over the same spatial

75 scale were also determined. The airborne measurements were obtained during an intensive

76 campaign from August to September 2013 in the Athabasca Oil Sands Region (AOSR) (Gordon

77 et al., 2015; Liggio et al., 2016; Li et al., 2017; Baray et al., 2018; Liggio et al., 2019) in northern

78 Alberta, Canada. Direct comparisons with modelled dry deposition estimates are made to assess

79 their uncertainties and the spatial-temporal scales of air pollutant impacts.

80 **2 Methods**

81 **2.1 Lagrangian Flight Design**

82   Details of the airborne measurement program have been described elsewhere (Gordon et

83 al., 2015; Liggio et al., 2016; Li et al., 2017; Liggio et al., 2019; Baray et al., 2018). Briefly, an

84 instrumented National Research Council of Canada's Convair-580 research aircraft was flown

85 over the AOSR in Alberta, Canada from August 13 to September 7, 2013. The flights were

86 designed to determine emissions from mining activities in the AOSR, assess their atmospheric

87 transformation processes and gather data for satellite and numerical model validation. Three

88 flights were flown to study transformation and deposition processes by flying a Lagrangian

89 pattern so that the same pollutant air mass was sampled at different time intervals downwind of

90 emission sources for a total of 4-5 hours and up to 107-135 km downwind of the AOSR sources.

91 Flights 7 (F7, Aug 19), 19 (F19, Sep 4) and 20 (F20, Sep 5) took place during the afternoon

92 when the boundary layer was well established. The flights were conducted in clear sky

93 conditions so wet deposition processes were insignificant. As shown in Figure 1, the aircraft

94 flew tracks perpendicular to the oil sands plume at multiple altitudes between 150 to 1400 m agl

95 and multiple intercepts of the same plume downwind. Vertical profiles conducted as spirals

96 were flown at the centre of the plume which provided information on the boundary layer height

97 and extent of plume mixing. The flight tracks closest to the AOSR intercepted the main

98 emissions from the oil sands operations; there were no other anthropogenic sources as the aircraft

99 flew further downwind of the AOSR.

2.2 Aircraft Measurements

100

A comprehensive suite of detailed gas- and particle-phase measurements were made from

101

102 the aircraft. Measurements pertaining to the analysis in this paper are discussed below.

103 **SO_2 and NO_y.** Ambient air was drawn in through a 6.35 mm (1/4") diameter PFA sampling line

104 taken from a rear-facing inlet located on the roof towards the rear of the aircraft. The inlet was

105 pressure-controlled to 770 mm Hg using a combination of a MKS pressure controller and a

106 Teflon pump. Ambient air from the pressure-controlled inlet was fed to instrumentation for

107 measuring SO_2 and NO_y. The total sample flow rate was measured at 4988 cm^3 min^{-1} of which

108 SO_2 and NO_y were 429 and 1085 cm^3 min^{-1}, respectively. SO_2 was detected via pulsed

109 fluorescence with a Thermo 43iTLE (Thermo Fisher Scientific, Franklin, MA, USA). NO_y (also

110 denoted as Total Oxidized Nitrogen (TON)) was measured by passing ambient air across a

111 heated (325ºC) molybdenum converter that reduces reactive nitrogen oxide species to NO. NO

112 was then detected through chemiluminescence with a modified Thermo 42iTL (Thermo Fisher

113 Scientific, Franklin, MA, USA) run in NO_y mode. An inlet filter was used for SO_2 to exclude

114 particles, but NO_y was not filtered prior to the molybdenum converter. NO_y includes NO, NO_2,

115 HNO_3 and other oxides of nitrogen such as peroxy acetyl nitrate and organic nitrates (Dunlea et

116 al., 2007; Williams et al., 1998). Although there was no filter on the NO_y inlet to exclude

117 particles, the inlet was not designed to sample particles (i.e. rear-facing PFA tubing). As a result,

118 pNO_3 was not included as part of NO_y (TON) The conversion efficiency of the heated

119 molybdenum converter and inlet transmission was evaluated with NO_2 and HNO_3 and found to

120 be near 100% and >90%, respectively. Previous studies conducted by Williams et al. (1998)

121 showed similar molybdenum converter efficiencies including that of n-propyl nitrate near 100%.

122 Interferences from alkenes or NH_3 were assumed to be negligible (Williams et al., 1998; Dunlea

123 et al. 2007). Species like NO_3 radical and N_2O_5 are expected to be low in concentration as they

124 photolyze quickly during daytime. Zeros were performed 3-5 times per flight for both the SO_2

125 and NO_y instruments by passing ambient air through an in-line Koby King Jr cartridge for ~5

126 minutes. For the NO_y measurements pre-reactor zeroes (dynamic instrument zero) were also

127 obtained periodically throughout each flight using either ambient air or a Koby King Jr. air

128 purifier. Multiple calibrations were conducted before, during and after the study using National

129 Institute Standards and Technology reference standards. Data were recorded at a time resolution

130 of 1 second and corrected for a sampling time delay of 1-3 seconds depending on the instrument.

131 Detection limits were determined as 2 times the standard deviation of the values acquired during

132 zeroes; NO_y was 0.09 ppbv and SO_2 was 0.70 ppbv (Table S1).

133 **Aerosols.** Multiple aerosol instruments sub-sampled from a forward facing, shrouded, isokinetic

134 particle inlet (Droplet Measurement Technologies, Boulder, CO, USA). A Time-of-Flight High

135 Resolution Aerosol Mass Spectrometer (AMS) (Aerodyne Research Inc.) was used to measure

136 non-refractory submicron aerosol components including pSO_4, pNO_3, pNH_4, and p-organics.

137 Details of the AMS and its operations have been published elsewhere (DeCarlo et al., 2006).

138 The instrument was operated in mass spectrometry V-mode with a sampling time resolution of

139 10 seconds. Filtered measurements were taken 4-5 times per flight to determine background

140 signals. Detection limits of 0.048, 0.036, 0.235 and 0.236 ug m^{-3} for pSO_4, pNO_3, pNH_4 and p-

141 organics were determined using 3 times the standard deviation of the average of filtered time

142 periods for all flights (Table S1). Ionization efficiency calibrations using monodisperse

143 ammonium nitrate were performed during the study with an uncertainty of ±9%. Data were

144 corrected for a sampling time delay of 10 seconds by comparing with faster response instruments

145 e.g. a wing-mounted Forward Scattering Spectrometer Probe Model 300 (FSSP-300) and an in-

146   board Ultra High Sensitivity Absorption Spectrometer (UHSAS) (both from Droplet

147   Measurement Technologies). The FSSP and UHSAS instruments measure particle diameters

148   that range from 300 nm – 20 µm and 50 nm - 1 µm, respectively. The AMS data were processed

149   using AMS data analysis software (Squirrel, version 1.51H and PIKA, version 1.10H). The

150   particle collection efficiency (CE) of the AMS was determined through comparisons of the total

151   AMS-derived mass with the mass estimated from the size distribution measurements of the

152   UHSAS assuming a density based on the chemical composition. The CE for F7 and F20 was 0.5

153   for both flights, and for F19 it was 1.0. The CE was applied to all AMS species for the duration

154   of each flight (Figure S1). Since the AMS measures only particle mass < 1 µm (PM_1) in

155   diameter, the mass of SO_4 formed through OH oxidation was scaled upward to account for all

156   particle sizes that H_2SO_4 vapor could potentially condense on. The scaling factor was

157   determined using the surface area ratio of PM_1/PM_{20} from the aircraft particle measurements,

158   assuming that the condensation process is approximately proportional to the surface area. . PM_1

159   measurements were from the UHSAS and PM_{20} were from the FSSP300. As the ratio did not

160   vary significantly in the plumes, one single value was used between each set of screens; in F19

161   the ratio between screens ranged from 0.6 to 0.8, in F20 the ratio ranged from 0.8 to 0.9, and in

162   F7 the ratio ranged from 0.7 to 0.9 (Liggio et al., 2016).

163   Measurements are discussed in terms of total oxidized sulfur (TOS, the sulfur mass in SO_2 from

164   the Thermo SO_2 instrument and particle-SO_4 (pSO_4) from the AMS instrument) and total

165   reactive oxidized nitrogen (TON, the nitrogen mass in reactive oxidized nitrogen species, from

166   the Thermo NO_y instrument, often denoted NO_y).

167   **Volatile Organic Compounds (VOCs).** Selected VOCs were used to estimate the OH

168   concentrations used for determining oxidation rates for SO_2. VOCs were measured with a proton

169 transfer reaction time-of-flight mass spectrometer (PTR-ToF-MS, Ionicon Analytik GmbH,

170 Austria) as well as through discrete canister grab samples. The PTR-ToF-MS and its operation,

171 along with the details of the canister sampling and lab analyses during the study were described

172 in detail previously (Li et al., 2017). Briefly, the PTR-ToF-MS used chemical ionization with

173 H_3O^+ as the primary reagent ion. Gases with a proton affinity greater than that of water were

174 protonated in the drift tube. The pressure and temperature of the drift tube region were

175 maintained at a constant 2.15 mbar and 60°C, respectively for an E/N of 141 Td (Townsend, 1

176 Td=10^{-17} V cm^2). E/N refers to the reduced electric field parameter in the drift tube; E is the

177 electric field and N is the number density of the gas in the drift tube. The E/N ratio can affect the

178 reagent ion distribution in the drift tube and VOC fragmentation (de Gouw and Warneke; 2007).

179 The protonated gases were detected using a high-resolution time of flight mass spectrometer at a

180 time resolution of 2 seconds. Instrumental backgrounds were performed in flight using a

181 custom-built zero-air generating unit. The unit contained a catalytic converter heated to 350°C

182 with a continuous flow of ambient air at a flow rate of one litre per minute. The data were

183 processed using Tofware software (Tofwerk AG). Calibrations were performed on the ground

184 using gas standard mixtures from Ionicon, Apel-Reimer and Scott-Marrin for 22 compounds.

185 The canister samples were collected in pre-cleaned and passivated 3L stainless steel canisters

186 that were subsequently sent to an analytical laboratory for GC-FID/MS analyses for a suite of

187 150 hydrocarbon compounds.

188 **Meteorology and aircraft state parameters.** Meteorological measurements have been

189 described elsewhere (Gordon et al., 2015). In brief, 3-D wind speed and temperature were

190 measured with a Rosemount 858 probe. Dew point was measured with an Edgetech hygrometer

191 and pressure was measured with a DigiQuartz sensor. Aircraft state parameters including

192   positions and altitudes were measured with GPS and a Honeywell HG1700 unit. All

193   meteorological measurements and aircraft state parameters were measured at a 1 s time

194   resolution.

195

196   **2.3 Mass transfer rates in the atmosphere**

197   Mass transfer rates (T) across flight screens (Figure 1) were determined using an

198   extension of the Top-down Emission Rate Retrieval Algorithm (TERRA) developed for emission

199   rate determination using aircraft measurements (Gordon et al., 2015). Briefly, at each plume

200   interception location, the level flight tracks were stacked to create a virtual screen.   Background

201   subtracted pollutant concentrations and horizontal wind speeds normal to the screen were

202   interpolated using kriging. The background for SO_2 was ~0 ppb and pSO_4 was $0.2 - 0.3$ µg m^{-3}

203   which was subtracted from the pSO_4 measurements before mass transfer rates were calculated

204   (Liggio et al., 2016). Integration of the horizontal fluxes across the plume extent on the screen

205   yields the transfer rate T in units of t hr^{-1} Using SO_2 as an example,

206   $$T_{SO_2} = \int_{s_1}^{s_2} \int_{z_1}^{z_2} C(s,z)u_n(s,z)dsdz \qquad\qquad (1)$$

207   where $C(s,z)$ is the background subtracted concentration at screen coordinate s and z, which

208   represent the horizontal and vertical axes of the screen. The $u_n(s,z)$ is the horizontal wind speed

209   normal to the screen at the same coordinates.

210   Since the lowest flight altitude was 150 magl, it was necessary to extrapolate the data to

211   the surface as per the procedures described previously (Gordon et al., 2015). Extrapolation to the

212   surface methods were compared and differences were included in the uncertainty estimates. The

213   main sources of SO_2 were from elevated facility stacks associated with the desulfurization of the

214 raw bitumen (Zhang et al., 2018). The stacks with the biggest SO_2 emissions range in height

215 from 76.2 to 183.0 m. Since the main source of SO_2 is from the elevated facility stacks, the

216 uncertainty for a single screen is estimated at 4% (Gordon et al., 2015). NO_y was also

217 extrapolated linearly to the surface and the mass transfer rates were similarly compared to other

218 extrapolation methods. NO_y sources include the elevated facility stacks and surface sources such

219 as the heavy hauler trucks operating in the surface mines. The uncertainty in the resulting

220 transfer rate **T** for a single screen is estimated to be larger at 8%, as a larger fraction of the NO_y

221 mass may be below the lowest measurement altitude (Gordon et al., 2015). Sulfur and nitrogen

222 data were also extrapolated linearly to background values from the highest altitude flight tracks

223 upwards to the mixed layer height, which was determined from vertical profiles of pollutant

224 mixing ratios, temperature and dew point (Table 1).

225   Changes in the mass transfer rate **T** (denoted **ΔT**) in units of t hr^{-1} were then calculated as

226 the differences in **T** between pairs of virtual screens. The uncertainty in **ΔT** was estimated as 8%

227 for **TOS** and 26% for **TON** as supported by emission rate uncertainties determined for box

228 flights (Gordon et al., 2015). The uncertainty analysis for box flights is applicable to **ΔT** here, as

229 both account for uncertainties with an upwind and a downwind screen. The **ΔT** uncertainties

230 were propagated through subsequent calculations.

231   Knowing the change in mass transfer rate **ΔT**, and accounting for the net rates of

232 chemical loss and formation between screens for SO_2 and pSO_4, the deposition rates (and

233 subsequently the deposition flux in tonnes S (or N) km^{-2} hr^{-1}, Section 2.4 were determined for the

234 sulfur compounds as follows:

235 $$\Delta T_{SO_2} = T_{SO_2}(t_2) - T_{SO_2}(t_1) = X_{SO2} - D_{SO2} \qquad (2)$$

236 $$\Delta T_{pSO_4} = T_{pSO_4}(t_2) - T_{pSO4}(t_1) = X_{pSO4} - D_{pSO4} \qquad (3)$$

237    $$\Delta T_{TOS} = T_{TOS}(t_2) - T_{TOS}(t_1) = -D_{TOS} \qquad \qquad (4)$$

238   where X_{SO2} is the rate of chemical reaction loss of sulfur mass in SO_2, X_{pSO4} is the rate of

239   chemical formation of sulfur mass as pSO_4, D_{SO2} and D_{pSO4} are deposition rates of sulfur mass in

240   SO_2 and pSO_4 respectively, and t_1 and t_2 are plume interceptions times at Screen 1 and Screen 2,

241   respectively. Note that the chemical loss rate of SO_2 is set to be equivalent to the formation rate

242   of pSO_4 ie. $X_{SO2} = X_{pSO4}$. Equation 4 for TOS can also similarly be written as shown in Equation

243   5.

244    $$\Delta T_{TOS} = \Delta T_{SO_2} + \Delta T_{pSO_4} = -D_{SO2} - D_{pSO4} \qquad \qquad (5)$$

245   Units in Equations 2 to 5 are all in t hr^{-1}. Reaction with the OH radical was considered to be the

246   most significant chemical loss of SO_2 and the most significant path for the formation of pSO_4.

247   X_{SO2} and X_{pSO4} were determined using estimated OH radical concentrations, which were

248   estimated using the methodology described in SI Section S4. Although TON encompasses a

249   range of different N species with expected differences in their deposition rates, it was not

250   possible to quantitatively separate their chemical formation/losses from their deposition rates

251   with this method. For total oxidized sulfur **TOS** (i.e., sulfur in SO_2 + pSO_4) and total oxidized

252   nitrogen **TON** (i.e., nitrogen in NO_y) the chemistry term is not relevant, and thus, the dry

253   deposition rate D_{TOS} was directly determined from ΔT_{TOS} using equation (4), and respectively for

254   **TON**.

255

256   **2.4 Dry deposition fluxes and dry deposition velocities**

257   Average dry deposition fluxes (F) for **TOS** and **TON** were obtained by dividing the

258   deposition rates D in t hr^{-1} with the footprint surface area of the plume between two adjacent

259   screens (Figure 1 grey shaded regions), as shown in Equation 6 for the dry deposition flux $\boldsymbol{F_{TOS}}$

260   of **TOS** (in t S km^{-2} hr^{-1}):

261          $$F_{TOS} = \frac{D_{TOS}}{Area} \qquad\qquad\qquad (6)$$

262   where the surface area, *Area*, was identified as the geographic area under the plume extending to

263   the edges of the plume where concentrations fell to background levels (i.e. SO_2 to ~0 ppb; SO_4

264   ~0.2 ug m^{-3}). This approach was similarly used to derive deposition fluxes from an air quality

265   model, Global Environmental Multiscale – Modelling Air-quality and Chemistry (GEM-MaCH)

266   (Moran et al., 2010; also see SI Section S5 for details). The geographic surface area uncertainty

267   is estimated at 5%. Dry deposition fluxes between the sources and the first screen were also

268   estimated using change in mass transfer rate $\boldsymbol{\Delta T}$ based on the extrapolated transfer rates back to

269   the source region ('extended' region). The surface area boundaries for these 'extended' regions

270   were determined using latitude and longitude coordinates that were weighted by emissions. This

271   was done by first using the average wind direction from Screen 1 and creating a set of parallel

272   back trajectories (~20) starting at different parts of Screen 1 back across the source region. For

273   **TON**, the NO_x emission sources along each back trajectory were weighted by their NO_x

274   emissions to obtain an emissions-weighted center location with latitude and longitude

275   coordinates for each back trajectory. The line connecting these emissions-weighted center

276   locations formed the boundary of the extended surface area. The extended surface area was

277   similarly determined for **TOS** based upon the known locations of the major SO_2 point sources.

278   The uncertainty of the 'extended' regions is estimated at 10% based on repeated optimizations of

279   the geographical area. Surface areas are visualized as grey shaded regions between screens in

280   Figure 1 and tabulated in SI Table S1.

281   Spatially-averaged dry deposition velocities, V_d, based on the aircraft measurements were

282   determined over the surface area between screens using average plume concentrations across

283   pairs of screens at about 40 meters above the ground for **SO₂** and **TON** (e.g. Equation 7 for SO₂

284   in units of cm s^{-1}). Although TOS includes the S in both SO_2 and pSO_4, only SO_2 is used in the

285   calculation of V_d since the deposition behaviour of gases and particles differ substantially, and

286   particles additionally have size-dependent deposition rates (Emerson et al., 2020). As the

287   dominant form of TOS is SO_2 (>92%) the deposition behaviour of TOS is expected to be largely

288   driven by that of SO_2. The measured TON does not include pNO_3.

289    $$V_d = \frac{F_{SO_2}}{[SO_2]} \qquad\qquad (7)$$

290   The largest source of uncertainty in V_d calculated this way was the determination of

291   concentration at 40 meters above the surface as the measurements were extrapolated from the

292   lowest aircraft altitude to the surface and interpolated concentrations were used. The

293   measurement-derived V_d are compared with those from the air quality model GEM-MACH

294   which uses inferential methods.

295

296   **2.5 Monte-Carlo simulations of dry deposition velocities using multiple resistance-based**

297   **parameterizations**

298   Parameterization of dry deposition in inferential algorithms is commonly based on a

299   resistance approach with dry deposition velocity depending on three main resistance terms as

300   below:

301
$$V_d = \frac{1}{R_a + R_b + R_c} \tag{8}$$

302

303   where R_a, R_b and R_c represent the aerodynamic, quasi-laminar sublayer and bulk surface

304   resistances respectively. Although these resistance terms are common among many regional air

305   quality models (Wu et al., 2018), the formulae used (and inputs in to these formulae) to calculate

306   the individual resistance terms differ significantly among the inferential deposition algorithms.

307   To assess the potential for a general underestimation of V_d across different inferential deposition

308   algorithms, and to compare with the aircraft-derived V_d, five different inferential deposition

309   algorithms, including that used in the GEM-MACH model for calculating V_d (Wu et al., 2018)

310   were incorporated into a Monte-Carlo simulation for V_d for SO_2. NO_y was not considered here,

311   as its measurement includes multiple reactive nitrogen oxide species with different individual

312   deposition velocities. We note that many of the inferential algorithms are based on observations

313   of SO_2 and O_3 deposition made at single sites, and the extent to which a chemical is similar to

314   SO_2 or O_3 features into its V_d calculation – the comparison thus has relevance for species aside

315   from SO_2. The five deposition algorithms considered are denoted ZHANG, NOAH-GEM,

316   C5DRY, WESLEY and GEM-MACH and are compared in Wu et al. (2018) (except the

317   algorithm in GEM-MACH). The five algorithms all use a big-leaf approach for calculating V_d

318   i.e. V_d is based on the resistance-analogy approach for calculating dry deposition velocity where

319   V_d is the reciprocal sum of three resistance terms R_a, R_b and R_c. Although the approach is

320   similar, the formulations of R_a, R_b and R_c between the algorithms are substantially different

321   (Table 1 in Wu et al., 2018). Results from Wu et al (2018) suggest that the differences in R_a+R_b

322   between different models would cause a difference in their V_d values on the order of 10-30% for

14

323   most chemical species (including SO_2 and NO_2), although the differences can be much larger for

324   species with near-zero R_c such as HNO_3.

325   To perform the simulations, formulae for the first four algorithms were taken from Wu et

326   al. (2018) and for GEM-MACH taken from Makar et al. (2018). The stomatal resistance in the

327   ZHANG algorithm was from Zhang et al. (2002). The GEM-MACH formula (Equation 8.7 in

328   the SI of Makar et al. (2018)) for mesophyll resistance R_{mx} contained a typo (missing the Leaf

329   Area Index (LAI)) and was corrected for as follows:

330    $R_{mx} = [LAI(H^*/3000 + 100\ f_0)]^{-1}$ (9)

331   Prescribed input values were constrained by the range of possible values consistent with the

332   conditions during the aircraft flights and are shown in SI Table S3 with associated references.

333   Calculations for the R_a term were based on unstable and dry conditions as observed during the

334   aircraft flights. The Monte-Carlo simulation generated a distribution of possible V_d values,

335   based on randomly generated values of the input variables to each algorithm and selected from

336   Gaussian distributions with a range of 3 sigma for all input parameters. All simulations were

337   performed with the same input values that were common between the algorithms.

338   **3 Results and Discussion**

339   **3.1 Meteorological and Emissions Conditions during the Transformation Flights**

340   Three aircraft flights, Flights 7 (F7), 19 (F19) and 20 (F20) were conducted in

341   Lagrangian patterns where the same plume emitted from oil sands activities was repeatedly

342   sampled for a 4-5 hour period and up to 107-135 km downwind of the AOSR. The first screen of

343   each flight captured the main emissions from the oil sands operations with no additional

344   anthropogenic sources between subsequent screens downwind. The main sources of nitrogen

345   oxides were from exhaust emissions from off-road vehicles used in open pit mining activities and

346   sulfur and nitrogen oxides from the elevated facility stack emissions associated with the

347   desulfurization of raw bitumen (Zhang et al., 2018). As depicted in Figure 1, F7 and F19

348   captured a plume that contained both sulfur and nitrogen oxides. The westerly wind direction

349   and orientation of the aircraft tracks on F20 resulted in the measurement of two distinct plumes;

350   one plume exhibited increased levels of sulfur and nitrogen oxides mainly from the facility

351   stacks, and the other plume contained elevated levels of nitrogen oxides, mainly from the open

352   pit mining activities, and no SO_2.

353   During the experiments, the dry deposition rates (**D**) (t hr^{-1}) were quantified under

354   different meteorological conditions and emissions levels of **TOS** and **TON** (**E_{TOS}** and **E_{TON}**) for

355   the three flights (see Table 1). These differences played important roles in the observed pollutant

356   concentrations and resulting dry deposition fluxes for F7, F19 and F20. Mixed layer heights

357   (MLH) were derived from aircraft vertical profiles that were conducted in the centre of the

358   plume at each downwind set of transects. The profiles of temperature, dew point temperature,

359   relative humidity and pollutant mixing ratios were inspected for vertical gradients indicating a

360   contiguous layer connected to the surface. The highest MLH was determined for F7 at 2500

361   magl whereas F19 had the lowest MLH at 1200 magl (Table 1). In F20, the MLH was 2100

362   magl. The combination of a high MLH in F7 with the highest wind speeds resulted in the lowest

363   pollutant concentrations of the three flights. In F19, lower wind speeds and the lowest mixed

364   layer heights led to the highest pollutant levels. F20 had emissions and meteorological

365   conditions that were in between F7 and F19 resulting in pollutant concentrations between those

366   of F7 and F19.

367   Emission rates of SO$_2$ and NO$_x$ (designated as E_{TOS} and E_{TON}) from the main sources in

368   the AOSR were estimated from the aircraft measurements and varied significantly between the

369   three flight days. The measurement-based emission rates of E_{TOS} and E_{TON} were taken from the

370   mass transfer rates of T_{SO2} and T_{NOy} (described in Methods) by extrapolating backwards to the

371   source locations in the AOSR using exponential functions (Figure 2, Section 3.2). For **TOS**, the

372   source location was set at 57.017N, -111.466W, where the main stacks for SO$_2$ emissions are

373   located. For **TON**, the source locations were determined from geographically weighted

374   locations. Emission rates E_{TOS} and E_{TON} for each flight are shown in Table 1.

375   Model-based E_{TOS} and E_{TON} were also obtained from the 2.5 km x 2.5 km gridded

376   emissions fields that were specifically developed for model simulations of the large AOSR

377   surface mining facilities (Zhang et al., 2018) i.e. Suncor Millenium, Syncrude Mildred Lake,

378   Syncrude Aurora North, Shell Canada Muskeg River Mine & Muskeg River Mine Expansion,

379   CNRL Horizon Project and Imperial Kearl Mine. The emissions fields have been used in GEM-

380   MACH (described in SI Section S5) to carry out a number of model simulations (Zhang et al.,

381   2018; Makar et al., 2018) including for the present study. In this work, emissions were summed

382   from various sources including offroad, point (Continuous Emissions Monitoring (CEMS)), and

383   point (non-CEMS) for the surface mines to obtain total AOSR hourly emission rates for the

384   flight time periods of interest (Table 2). The standard deviations reflect the emissions variations

385   during the simulated flight.

386   **3.2 Mass Transfer Rates**

387   The mass transfer rates T (in t hr^{-1}) across the virtual flight screens for all three flights are

388   shown for **TOS** and **TON** in Figure 1 and plotted in Figure 2. In F20, two distinct **TON** plumes

389   were observed, allowing separate T calculations for **TON**. Monotonic decreases in T were

390 observed for both **TOS** and **TON** during transport downwind in all flights, clearly showing dry

391 depositional losses. The deposition rate D (Methods, Section 2.3) was used to estimate the

392 cumulative deposition of **TOS** and **TON** as a fraction of E_{TOS} or E_{TON} and is shown in Figure 3

393 for F7, F19 and F20 for transport distances of up to 107-135 km downwind of the sources.

394 Curves were fitted to the **TOS** and **TON** dry deposition cumulative percentages from which $d_{1/e}$

395 and τ were determined (SI Table S1). The transport e-folding distance ($d_{1/e}$) was determined

396 where 63.2% of E_{TOS} (or E_{TON}) was dry deposited, i.e., $\sum_{d=0}^{d_{1/e}} D(d) = 0.368 E_{TOS}$. The

397 atmospheric lifetimes (τ) were derived as $\tau = d_{1/e}/u$, where u was the average wind speed across

398 the distance $d_{1/e}$. These estimates were compared with predictions from the regional air quality

399 model GEM-MACH (Makar et al., 2018; Moran et al., 2010; SI Section S5) using facility

400 emission rates (Table 2). For **TOS** during F19, (Figure 3b, e), the observed cumulative

401 deposition at the maximum distance accounted for 74±5% vs. the modelled 21% of $E_{TOS.}$ The

402 measurements indicate that the cumulative deposition of TOS was due mostly to SO_2 dry

403 deposition where SO_2 was ~100% of TOS closest to the oil sands sources decreasing to 94%

404 farthest downwind. Although the modelled cumulative deposition of TOS was significantly

405 lower than the observations, the fractional deposition of SO_2 was similar, decreasing from

406 ~100% to 95% of TOS. Fitting a curve to D and interpolating the cumulative deposition fraction

407 to the 63.2% E_{TOS} loss leads to a $d_{1/e}$ of 71±1 km, versus 500 km for the model prediction.

408 Under the prevailing wind conditions, the observed distance indicates a τ for **TOS** of

409 approximately 2.2 hours, whereas the model prediction indicated 16 hours. Large observation-

410 based values and model prediction differences in lifetime were also evident for the other flights

411 (SI Table S1). Clearly, the model predictions significantly underestimated deposition and vastly

412 overestimated $d_{1/e}$ and τ. The observation-based values for τ are also lower than average

413   lifetimes of 1–2 days for SO_2 and 2–9 days for pSO_4 derived from global models (Chin et al.,

414   2000; Benkovitz et al., 2004; Berglen et al., 2004), which include the effects of wet deposition

415   and chemical conversion for SO_2, thus making their implicit residence times with respect to dry

416   deposition even longer.

417   For **TON** in F19 (Figure 3h, l), the observed cumulative deposition accounted for

418   49±11% of E_{TON} at the maximum flight distance, versus 19% predicted by the model. Similar

419   model underestimates for cumulative deposition fractions were found for F7 and F20.

420   Extrapolating to the 63.2% cumulative deposition fraction, $d_{1/e}$ was estimated to be 190±7 km for

421   F19 versus a predicted 650 km from the model, implying a τ of approximately 5.6 hours for the

422   measurement-based results and 23 hours for the model prediction. Again, analogous differences

423   for F7 and F20 were found (SI Table S1). Similar to TOS, the measurement-based $d_{1/e}$ and τ

424   values for TON were significantly smaller than commonly accepted lifetimes of a few days for

425   nitrogen oxides in the boundary layer (Munger et al., 1998).

3.3 Dry Deposition Fluxes F

427   Using the deposition rate D (in tonnes S or N hr^{-1}), the average dry deposition fluxes, F

428   (in tonnes S or N km^{-2} hr^{-1}), were calculated by dividing D by the plume footprint surface areas

429   estimated by extending to the plume edges where the concentrations fell to background levels

430   (Methods, Section 2.4). These footprints are shown as the gray shaded geographic areas in

431   Figure 1, totaling 3500, 5700 and $4200 km^2$ for F7, F19, and F20 plumes, respectively; see SI

432   Table S1 for **TON** plume areas). Figure 4a shows F_{TOS} values for all three flights, exhibiting

433   exponential decreases with increasing distance away from the sources and showing e-folding

434   distances for F_{TOS} of 18, 27, and 55 km for F7, F19, and F20, respectively. More than 90% of

435   the decreases in F_{TOS} were accounted for by F_{SO2}. Similarly, F_{TON} decreased exponentially with

436   increasing transport distances in all flights (Figure 4c), exhibiting e-folding distances of 18 and

437   33 km for F7 and F19, and 55 and 189 km for the south and north **TON** plumes during F20,

438   respectively. These e-folding distances were similar to those for F_{TOS}, indicating similar rates of

439   decreases in F_{TON} with transport distances.

440   The potential for other processes to contribute to the derived TOS and TON fluxes were

441   considered including losses from the boundary layer to the free troposphere and re-emission of

442   TOS or TON species from the surface back to the gas-phase. Two different approaches, a finite

443   jump model and a gradient flux approach (Stull, 1988; Degrazia et al., 2015), were used to

444   estimate the potential upward loss across the interface between the boundary layer and the free

445   troposphere for sulfur and nitrogen. In both approaches, the upward S flux was a minor loss at <

446   45 g km^{-2} hr^{-1}, about 3 orders of magnitude lower than the several to many kg km^{-2} hr^{-1}

447   horizontal advectional transport that were determined using TERRA. For N, the upward flux

448   was estimated to be ~570 g km^{-2} hr^{-1}, so although a larger flux than S, it is about factor of 18

449   lower than the TON fluxes derived from observations.

450   As expected from the τ and transport e-folding distance $d_{1/e}$ comparisons, the GEM-

451   MACH model F_{TOS} were significantly lower than the measurement-based F_{TOS} results (Figure

452   4a), with the model F_{TOS} e-folding distances usually large: 133, 797, and 57 km for F7, F19, and

453   F20, respectively, or 7.4, 29.5, and 1.1 times longer than the corresponding measurement results.

454   Part of the differences between model and measurement F_{TOS} could be explained by differences

455   in actual versus model emissions, E_{TOS} (Tables 1 vs 2). To remove the influence of emissions,

456   an emission-normalized flux (=F_{TOS}/E_{TOS} and F_{TON}/E_{TON}) was calculated for both measurement

457   and model (SI Figure S2). Figure 4b shows the ratios of measurement to model normalized

458   emissions for TOS. The model emission-normalized fluxes F_{TOS}/E_{TOS} were lower than the

459   measurement-based values by factors of 2.5-14, 1.8-3.4, and 2.0-3.0 for F7, F19, and F20,

460   respectively, decreasing with increased transport distances. However, they coalesce to a factor

461   of 2 at the furthest distances sampled by the aircraft, indicating that the model F_{TOS} estimates

462   were biased low by similar factors. The decreasing trends suggest that at distances further

463   downwind, model fluxes may exceed measurement-based fluxes, albeit at magnitudes lower than

464   those shown in Figure 4a, which is consistent with earlier study results (Makar et al., 2018). For

465   F_{TON}, the model-predicted values were also lower than the measurement results, especially near

466   the sources (Figure 4c), and showed little variation with transport distances from the oil sands

467   sources for all flights, in strong contrast to the exponential decays observed from the aircraft.

468   However, the emission-normalized fluxes ($=F_{TON}/E_{TON}$) for the model approached those from

469   measurements within maximum flying distances for F19 and F20, although still significantly

470   lower for F7 (>10x) (Figure 4d).

471   **3.4 Dry Deposition Velocities V_d**

472   The shorter $d_{1/e}$ and τ, and larger deposition fluxes F near the sources determined from

473   the aircraft measurements compared to predictions by the GEM-MACH model indicate that the

474   model dry deposition velocities V_d was underestimated. Gas-phase V_d in the model is predicted

475   with a standard inferential "resistance" algorithm (Wesley, 1989; Jarvis, 1976), with resistance to

476   deposition calculated for multiple parameters including aerodynamic, quasi-laminar sublayer and

477   bulk surface resistances (Baldocchi, 1987). To demonstrate the model underestimation in V_d,

478   comparisons between the measurement-based and model V_d were made where an evaluation of

479   V_d for **TOS** and **TON** was possible. All F_{SO2} were converted into $V_{d\text{-}SO2}$ by dividing F_{SO2} by

480   interpolated SO_2 concentrations at 40 meters above ground, averaging 1.2±0.5, 2.4±0.4, and

481   3.4±0.6 cm s^{-1} for F7, F19 and F20, respectively, across the plume footprints (Methods, Section

482   2.4 and SI Table S2). The corresponding model $V_{d\text{-}SO2}$ derived in the same way as the

483   observations was 0.72, 0.63, and 0.58 cm s^{-1}, 1.7-5.4 times lower than observations (SI Section

484   S5; SI Table S2). Interestingly, the median V_d for SO$_2$ of 4.1 cm s^{-1} determined using eddy

485   covariance/vertical gradient measurements from a tower in the AOSR is higher than the mass

486   balanced method showing an even larger discrepancy compared to the model (SI Section S3;

487   Figure S5). Similarly, derived $V_{d\text{-}TON}$ averaged 2.8±0.8, 1.6±0.5, 4.7±1.4 and 2.2±0.7 cm s^{-1} F7,

488   F19, F20 south plume, and F20 north plume, respectively (SI Table S2), 1.2-5.2 times higher

489   than the corresponding modelled $V_{d\text{-}TON}$ of 1.4, 1.3, 0.92, and 0.90 cm s^{-1}.

490   Using the observations, it was not possible to derive individual TON deposition rates

491   separate from their chemical formation/losses. In previous modelling work, Makar et al. (2018),

492   use the GEM-MACH model and describe the relative contributions of different TOS and TON

493   species towards total S and N deposition in the AOSR. TON was dominated by dry NO$_2$ (g)

494   deposition fluxes close to the sources (>70% of total N close to the sources), and dry HNO$_3$ (g)

495   deposition increases with increasing distance from the sources (remaining $< 30\%$ of total N), and

496   other sources of TON having minor contributions to deposition ($< 10\%$). Although TON

497   encompasses a range of different N species with expected differences in their deposition rates,

498   comparisons of $V_{d\text{-}TON}$ with the model show, nevertheless, that overall large differences do exist.

499   **3.5 Monte-Carlo simulations of V_d for SO$_2$**

500   To further demonstrate observation-model differences, V_d distributions of SO$_2$ from five

501   common inferential dry deposition algorithms (Wu et al., 2018; Makar et al., 2018) were

502   determined for the conditions encountered during the flights using a Monte-Carlo approach as

503   described in Methods, Section 2.5). Results for the V_d simulations algorithms are shown in

504   Figure 5a. Histograms for all five algorithms have peak V_d values at ~1 cm s^{-1} or lower.

505   Probability distributions for the individual resistance terms, R_a, R_b, and R_c showed that the

506   dominant resistance driving V_d was the R_c term (SI Figure S3). Also shown in Figure 5a are the

507   measurement-derived V_d for Flights 7, 19 and 20, and that from the Oski-ôtin ground site. The

508   observed V_d values are larger than the V_d values for most of the simulations, with the exception

509   of Flight 7, where the Zhang et al. (2002), NOAH-GEM (Wu et al., 2018) and C5DRY (Wu et

510   al., 2018) algorithms' distributions agree with the observations. All algorithms are biased low

511   relative to the observations for the remaining flights, and the Oski-ôtin ground site.   It is noted

512   that the ground-site observations that were derived using a standard flux tower methodology (SI

513   Section S3) at a single site, appeared to be higher than all other V_d; nevertheless, these

514   observations are closer to the aircraft values than the algorithm estimates. These results indicate

515   that an underestimation of V_d relative to both aircraft and ground based measurements in the

516   AOSR is not unique to the GEM-MACH model or its dry deposition algorithm; similar results

517   would occur with the other algorithms included in the Monte-Carlo simulations, all of which are

518   used within other regional models.

519   To investigate the possible reasons behind the low model V_d relative to the observations,

520   a series of sensitivity tests using SO_2 were conducted. Differences in model V_d have been shown

521   to be mainly due to differences in the calculated R_c (Wu et al., 2018), and sensitivity tests here

522   indicated that R_c is particularly sensitive to the cuticular resistance R_{cut}. Hence, factors causing

523   R_{cut} to change can have significant impact on model V_d. In some of the algorithms, R_{cut} and

524   other resistance terms are dependent on the effective Henry's Law constant K_H^* for SO_2. The

525   Monte-Carlo simulations for Figure 5 assumed a surface pH= 6.68 resulting in a K_H^* of 1×10^5 for

526   SO_2. Additional Monte-Carlo simulations were performed for the GEM-MACH dry deposition

527   algorithm by adjusting K_H^* assuming different pH with small variations from a pH=6.68

528   significantly changing R_c, R_{cut}, and V_d (SI Figure S4). In Figure 5b – red dashed line, with a

529   surface pH change from 6.68 to 8, consistent with possible alkaline surfaces in the AOSR

530   (Makar et al., 2018), in the GEM-MACH simulation, the V_d distribution is moved to larger

531   values) with its peak value shifting from 0.6 to 1.4 cm s^{-1}. These results show that model V_d may

532   be highly sensitive to assumed surface pH, at least when using some inferential dry deposition

533   algorithms which are pH-dependent. However, Figure 5b shows that this pH-associated increase

534   in V_d is still insufficient to encompass the range of measurement-derived V_d. Increasing pH to 8

535   for the GEM-MACH simulation reduces R_{cut}, hence R_c, to values much smaller than R_a and R_b,

536   suggesting that model V_d cannot further increase without reductions in both R_a and R_b. In other

537   words, R_a and R_b were probably overestimated in the current deposition velocity algorithms. By

538   using the Zhang et al. (2002) R_a and the NOAH-GEM (Wu et al., 2018) R_b parameterizations in

539   the GEM-MACH algorithm, a further shift of the GEM-MACH V_d distribution to larger values

540   was found, with the range encompassing most of the observations (Figure 5b, pink dashed line).

541   Using the Zhang and NOAH-GEM parameterizations, rather than the GEM-MACH

542   parameterization, would decrease the R_a and R_b for the momentum, heat and moisture fluxes as

543   well, but still remain within the range of what is expected based on published parameterizations

544   (Wu et al., 2018 and references therein).

545   The potential for re-emission of TOS and TON species was also considered. Fulgham et

546   al. (2020) report that the bidirectional fluxes of volatile organic acids are driven by an

547   equilibrium partitioning between surface wetness and the atmosphere. The observations

548   presented here represent the net flux of all processes including the effects of deposition and any

549   potential re-emissions of TOS and TON compounds should this process occur. As the results

550   show a net downward flux (i.e. net deposition), if any re-emission was occuring, it would be

551 smaller than the deposition fluxes observed here, which are themselves higher than shown by

552 currently available deposition algorithms. This implies that the deposition part of the flux must

553 be even larger than the net observed flux and the measured net fluxes presented here should then

554 be considered as minimum values. The current deposition algorithms do not include

555 bidirectional fluxes for inorganics, and adjustments related to pH in some situations may not be

556 sufficient to parameterize deposition fluxes. A bidirectional approach may be needed that would

557 include not only [H$^+$], but surface heterogeneous reactions, to determine near-surface equilibrium

558 concentrations of co-depositing gases such as ammonia and nitric acid.

559   It is clear from the Monte-Carlo simulations for SO_2 $\boldsymbol{V_d}$ comparisons, inferential dry

560 deposition algorithms as used in regional and global chemical transport models need to be further

561 validated and improved, especially over large geographic regions. Here, the role of pH was

562 identified for improvement in some algorithms along with possible improvement in aerodynamic

563 and quasi-laminar sublayer resistance parameters. Yet, for other algorithms and for **TON**

564 compounds, the model low-biases in $\boldsymbol{V_d}$ remain to be investigated.

565   The underestimates suggest that the applications of these algorithms in regional or global

566 models may significantly underestimate predictions of **TOS** dry depositional loss from the

567 atmosphere. Underestimates in $\boldsymbol{V_d}$ are the result of a combination of uncertainties in the

568 parameterizations of each algorithm. In the case of the algorithm used in GEM-MACH, by

569 adjusting the assumed surface pH from 6.68 to 8 (justifiable given the considerable dust

570 emissions in the region (Zhang et al., 2018)), the model $\boldsymbol{V_d}$ moved closer to the aircraft-derived

571 values (Figure 5b), reducing the model-observation gap by approximately 2/3. In addition,

572 substituting the aerodynamic resistance and quasi-laminar sublayer resistance parameterizations

573 in the GEM-MACH algorithm with that from Zhang et al. (2002) and NOAH-GEM (Wu et al.,

574   2018), respectively, resulted in a further increase in the model V_d distribution that encompasses

575   most of the observations (Figure 5b). Clearly, different algorithms respond differently to

576   changes in the parameterizations, and validation and adjustment to each algorithm needs

577   measurement-based results over large regions such as derived here.

578

579   **4 Conclusions**

580   The atmospheric transport distances and lifetimes $\boldsymbol{d_{1/e}}$ and $\boldsymbol{\tau}$ determined from the aircraft

581   measurements are substantially shorter than the GEM-MACH model predictions, and the dry

582   deposition fluxes $\boldsymbol{F}$ and velocities and $\boldsymbol{V_d}$ near sources are larger compared to the predictions by

583   GEM-MACH and five inferential dry deposition velocity algorithms, respectively. There are

584   important implications for these measurement-model discrepancies. Such discrepancies indicate

585   that regional or global chemical transport models using these algorithms are biased low for local

586   deposition and high for long-range transport and deposition, and **TOS** and **TON** loss from the

587   atmosphere are significantly under-predicted, resulting in overestimated lifetimes. While the

588   measurements took place over a relatively short time period, these results indicate that TOS and

589   TON may be removed from the atmosphere at about twice the rate as predicted by current

590   atmospheric deposition algorithms. This, in turn, implies a potentially significant impact on

591   deposition over longer time scales (potentially weeks to months) and relevance towards

592   cumulative environmental exposure metrics such as critical loads and their exceedance. A faster

593   near-source deposition velocity for emitted reactive gases may imply less S and N mass being

594   available for long range transport, reducing concentrations and deposition further downwind.

595   The near-source higher deposition velocity, thus has the important implication of a reduction in

596   more distant and longer timescale deposition for locations further from the sources. Moreover,

597   emissions assessed through network measurements or budget analysis of atmospheric **TOS** and

598   **TON** (Sickles and Shadwick, 2015; Paulot et al., 2018; Berglen et al., 2004) may be

599   underestimated due to lower V_d used in these estimates, and may require reassessing the

600   effectiveness of control policies. Shorter τ for **TOS** and **TON** reduces their atmospheric spatial

601   scale and intensity of smog episodes, potentially reducing human exposures (Moran et al., 2010).

602   Importantly, shorter τ for **TOS** and **TON** reduces their contribution to atmospheric aerosols;

603   consequently, the negative direct and indirect radiative forcing from these sulfur and nitrogen

604   aerosols are reduced, reducing their cooling effects on climate (Solomon et al., 2007). These

605   impacts suggest that more measurements to determine τ and F for these pollutants across large

606   geographic scales and different surface types are necessary to better quantify their climate and

607   environmental impacts in support of policy. While in the past such determination was difficult

608   and/or impossible, the present study provides a viable methodology to achieve such a goal.

609

610

611 **Table 1.** Average observed meteorological conditions and facility emission rates of **TOS** (E_{TOS})
612 and **TON** (E_{TON}), (determined from extrapolated (to distance=0) transfer rates; Figure 1) for
613 **TOS** and **TON** during the F7, F19 and F20 flights. SP=south plume; NP=north plume.

Flight	Date	Time (UTC)	Mean wind speed (m/s)	Mean wind direction (°)	Mixed layer height (m agl)	E_{TOS} (t/hr)	E_{TON} (t/hr)
7	Aug 19/13	2007–0108	13.0±1.0	256±11.7	2500±100	3.4	1.2
19	Sep 4/13	1854–2353	9.5±1.9	218±16	1200±100	18.5	3.9
20	Sep 5/13	1933-2436	8.9±1.2	281±11	2100±100	5.8	2.2 (SP) 1.2 (NP)

614

615 **Table 2**. Model average meteorological conditions and facility emission rates of **TOS** (E_{TOS}) and
616 **TON** (E_{TON}) during the F7, F19 and F20 flights as described above. SP=south plume; NP=north
617 plume.

Flight	Date	Time (UTC)	mean wind speed (m/s)	mean wind direction (°)	mixed layer height (m agl)	E_{TOS} (t/hr)	E_{TON} (t/hr)
7	Aug 19/13	2007–0108	12.6±0.3	253±5.0	1670±80	3.8	2.9
19	Sep 4/13	1854–2353	8.1±1.0	225±4.6	1450±43	4.3	2.4
20	Sep 5/13	1933-2436	9.1±0.7	275±1.6	1590±42	3.7	1.5 (SP) 0.9 (NP)

618
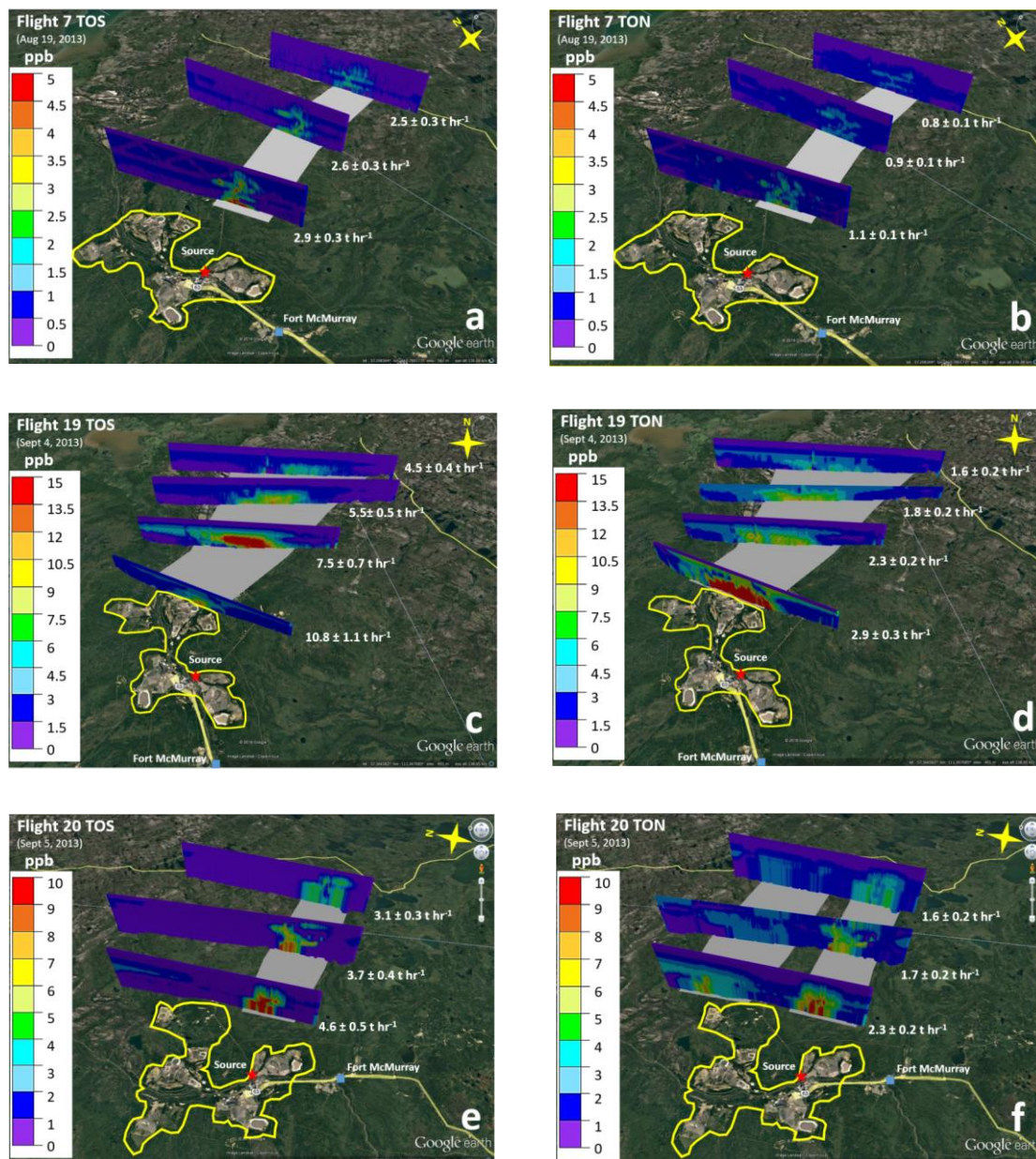
Figure 1. **TOS** (total oxidized sulfur) and **TON** (total oxidized nitrogen) plumes downwind of the AOSR during three Lagrangian flights, F7, F19 and F20. The AOSR facilities are enclosed by the yellow outline. The transfer rates T in t S or N hr^{-1} across each screen are shown. The grey shaded surface areas are identified as the geographic footprint under the plumes. Data: Google Image © 2018 Image Landsat / Copernicus.
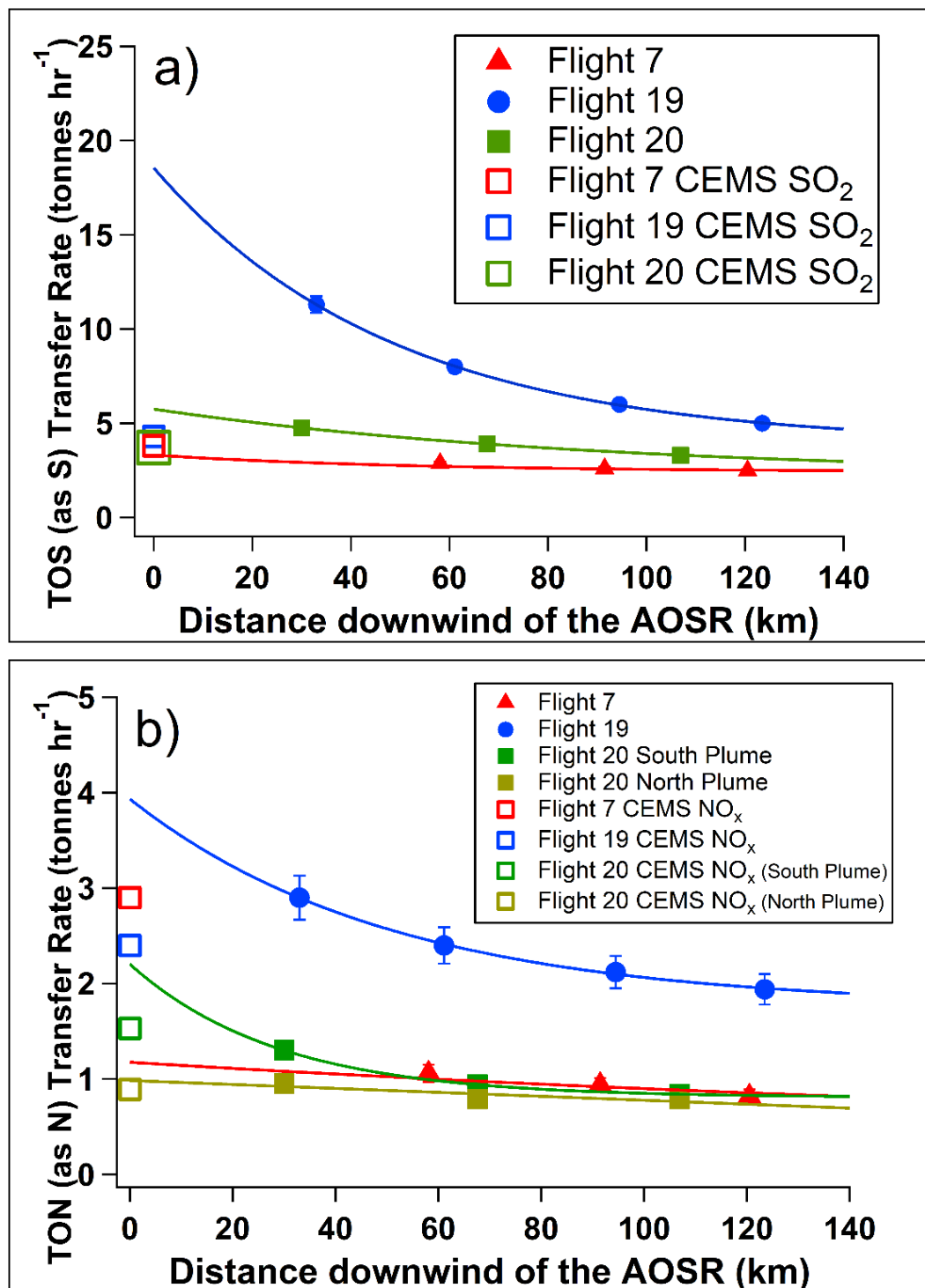
Figure 2. TERRA-derived transfer rates of (a) **TOS** and (b) **TON** for F7, F19 and F20. The vertical bars indicate the propagated uncertainties. The model emission rates E_{TOS} and E_{TON} are shown by the open symbols.

630
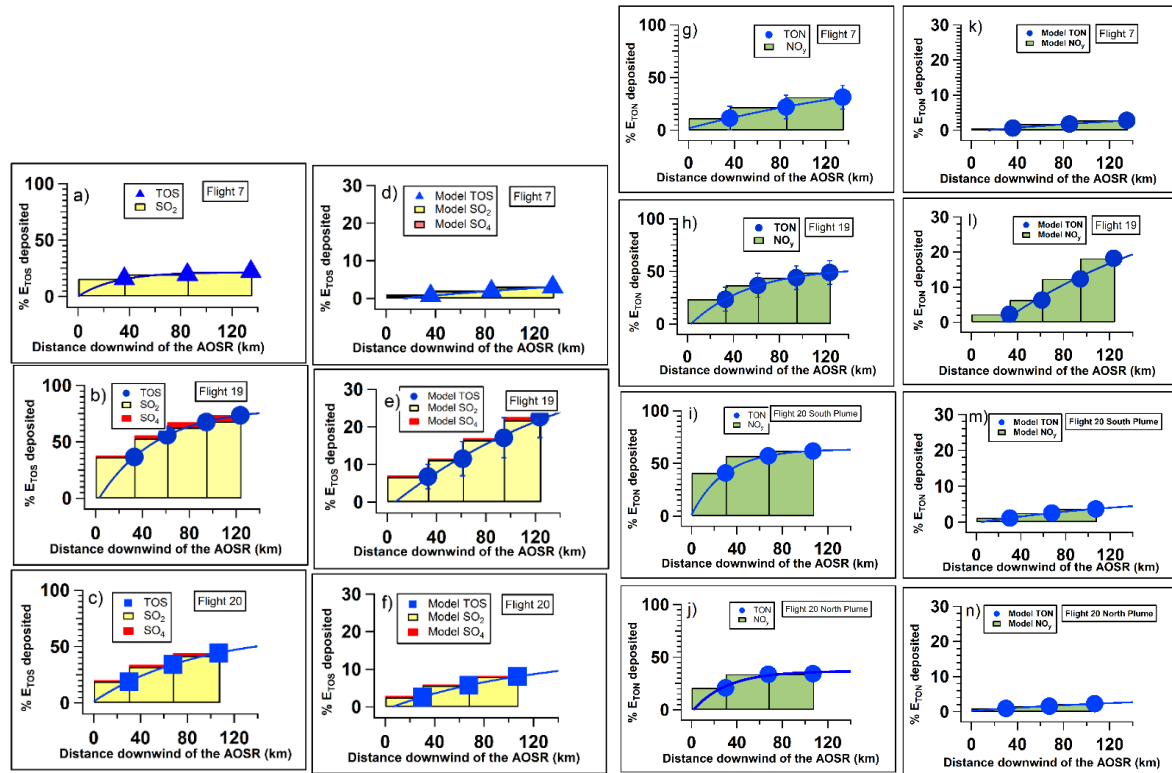
Figure 3. Cumulative dry deposition as a percentage of emissions E_{TOS} (a to f) or E_{TON} (g to n) for F7, F19 and F20 measurements with corresponding GEM-MACH model predictions. The bars show the dry deposition due to SO_2 and pSO_4. The curves were fitted to the **TOS** and **TON** dry deposition percentages from which $d_{1/e}$ and τ were determined.

635
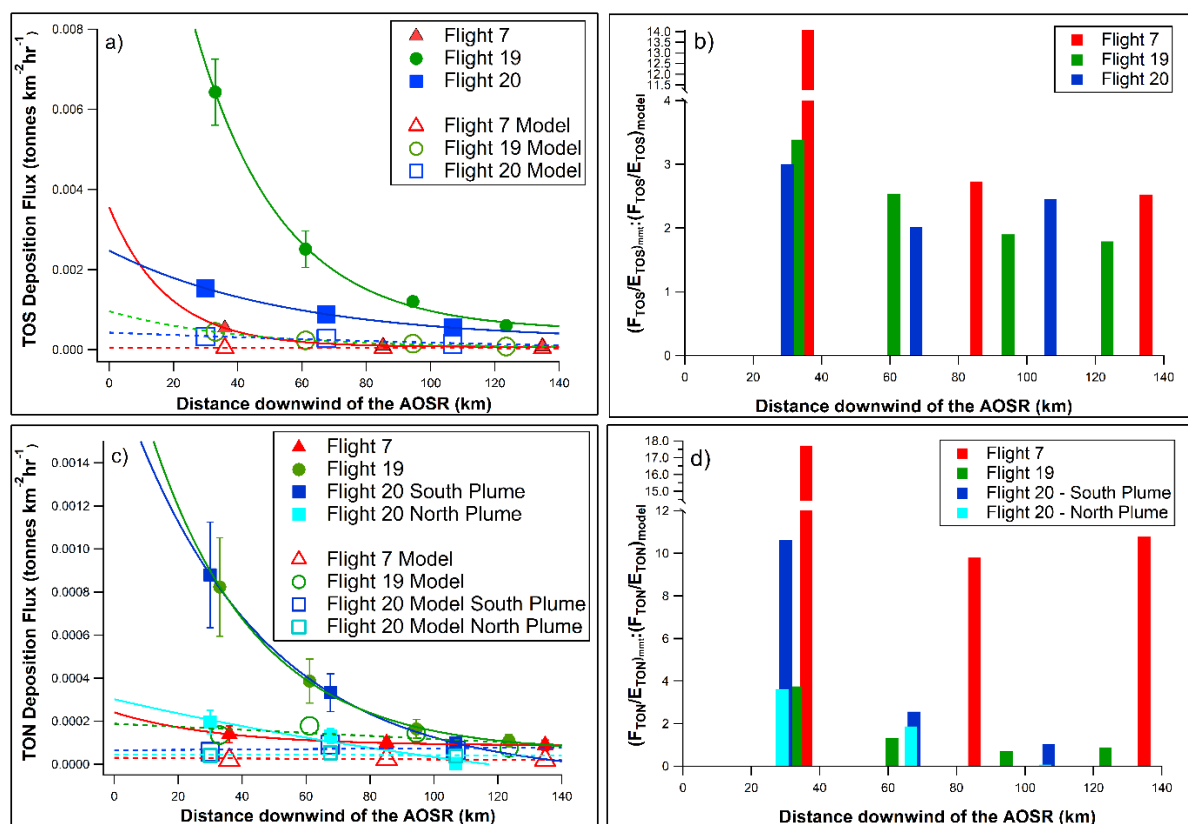
Figure 4. Dry deposition fluxes F_{TOS} and F_{TON} (**in t km^{-2} hr^{-1}**) determined from measurements (solid symbols) and GEM-MACH model predictions (open symbols). (a) F_{TOS}, (b) ratios of measurement to model normalized emissions F_{TOS}/E_{TOS}, (c) F_{TON}, and (d) ratios of measurement to model normalized emissions F_{TON}/E_{TON}.

640

32
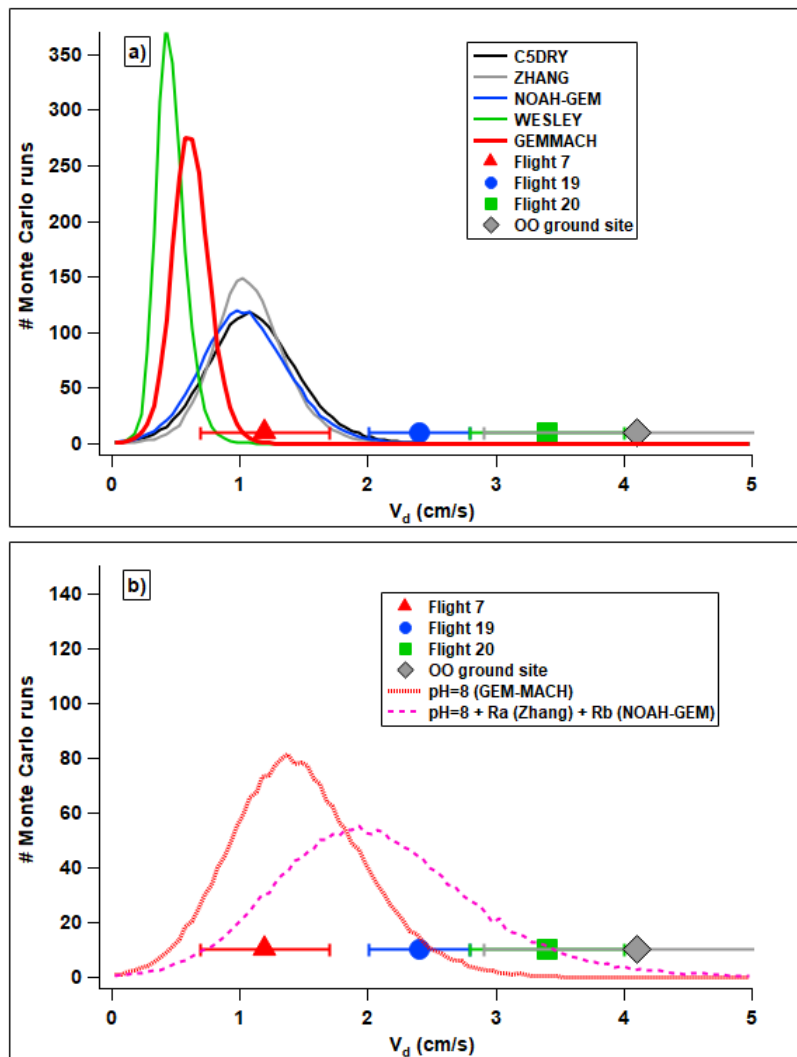
Figure 5. (a) Distributions of V_d for SO_2 from Monte-Carlo simulations using 5 different deposition parameterizations (Wu et al., 2018; Makar et al., 2018) and (b) Monte-Carlo simulations for the GEM-MACH algorithm using a pH=8 and using a pH=8 plus replacing the GEM-MACH algorithm R_a and R_b formulae with that from Zhang et al. (2002) and NOAH-GEM (Wu et al., 2018), respectively. Aircraft-derived V_d for F7, F19 and F20 as well as the median value for the Oski-ôtin ground site (SI Figure S5) are shown in both (a) and (b) for comparison.

References

Aubinet, M., Vesala, T. and Papale, D. (Eds.): Eddy Covariance. Springer Atmospheric Sciences, Springer, Dordrecht, 2012.

Baldocchi, D.D., Vogel, C.A., and Hall, B.: A canopy stomatal resistance model for gaseous deposition to vegetated surfaces, Atmos. Env., **21**, 91-101, https://doi.org/10.1016/0004-6981(87)90274-5, 1987.

Baray, S., Darlington, A., Gordon, M., Hayden, K.L., Leithead, A., Li, S.-M., Liu, P.S.K., Mittermeier, R.L., Moussa, S.G., O'Brien, J., Staebler, R., Wolde, M., Worthy, D. and McLaren, R.: Quantification of methane sources in the Athabasca Oil Sands Region of Alberta by aircraft mass balance, Atmos. Chem. Phys., **18**, 7361-7378, https://doi.org/10.5194/acp-18-7361-20182018.

Benkovitz, C.M., Schwartz, S.E., Jensen, M.P., Miller, M.A., Easter, R.C. and Bates, T.S.: Modeling atmospheric sulfur over the Northern Hemisphere during the Aerosol Characterization Experiment 2 experimental period, J. Geophys. Res., **109**, D2220, https://doi.org/10.1029/2004JD004939, 7, 2004.

Berglen, T.F., Berntsen, T.K., Isaksen, I.S.A. and Sundet, J.K.: A global model of the coupled sulfur/oxidant chemistry in the troposphere: The sulfur cycle, J. Geophys. Res., **109**, D19310, https://doi.org/10.1029/2003JD003948, 2004.

Bobbink, R., Hicks, K., Galloway, J., Spranger, T., Alkemade, R., Ashmore, M., Bustamante, M., Cinderby, S., Davidson, E., Dentener, F., Emmett, B., Erisman, J-W., Fenn, M., Gilliam, F., Nordin, A., Pardo, L. and De Vries, W.: Global assessment of nitrogen deposition effects on terrestrial plant diversity: a synthesis, Ecol. Appl. **20**, 30-59, https://doi.org/10.1890/08-1140.1, 2010.

Brook, J.R., Di-Giovanni, F., Cakmak, S. and Meyers, T.P.: Estimation of dry deposition velocity using inferential models and site-specific meteorology – uncertainty due to siting of meteorological towers, Atmos. Environ., **31**, 3911-3919, https://doi.org/10.1016/S1352-2310(97)00247-1, 1997.

Chin, M., Savoie, D.L., Huebert, J., Bandy, A.R., Thornton, D.C., Bates, T.S., Quinn, P.K., Saltzman, E.S. and De Bruyn, W.J.: Atmospheric sulfur cycle simulated in the global model GOCART: Comparison with field observations and regional budgets, J. Geophys. Res., **105**, 24689-24712, https://doi.org/10.1029/2000JD900384, 2000.

Christian, G., Ammann, M., D'Anna, B., Donaldson, D.J. and Nizkorodov, S.A.: Heterogeneous photochemistry in the atmosphere, Chem. Rev. **115**, 4218-4258, https://doi.org/10.1021/cr500648z, 2015.

DeCarlo, P.F. , Kimmel, J.R., Trimborn, A., Northway, M.J., Jayne, J.T., Aiken, A.C., Gonin, M., Fuhrer, K., Horvath, T., Docherty, K.S., Worsnop, D.R., Jimenez, J.L.: Field-deployable, high-resolution, time-of-flight aerosol mass spectrometer, Anal. Chem., 8281-9289, https://doi.org/10.1021/ac061249n, 2006.

de Gouw, J. and Warneke, C.: Measurements of volatile organic compounds in the earth's atmosphere using proton-transfer-reaction mass spectrometry, Mass Spectrom. Rev., 26, 223-257, https://doi.org/10.1002/mas.20119, 2007.

Degrazia, G.A., Maldaner, S., Buske, D., Rizza, U., Buligon, L., Cardoso, V., Roberti, D.R., Acevedo, O., Rolim, S.B.A. and Stefanello, M.B.: Eddy diffusivities for the convective boundary layer derived from LES spectral data, Atmos. Pollut. Res., **6**, 605-611, https://doi.org/10.5094/APR.2015.068, 2015.

Dentener, F., Drevet, J., Lamarque, J.F., Bey, I., Eickhout, B., Fiore, A.M., Hauglustaine, D., Horowitz, L.W., Krol, M., Kulshrestha, U.C., Lawrence, M., Galy-Lacaux, C., Rast, S., Shindell, D., Stevenson, D., Van Noije, T., Atherton, C., Bell, N., Bergman, D., Butler, T., Cofala, J., Collins, B., Doherty, R., Ellingsen, K., Galloway, J., Gauss, M., Montanaro, V., Müller, J.F., Pitari, G., Rodriguez, J., Sanderson, M., Solmon, F., Strahan, S., Schultz, M., Sudo, K., Szopa, S. and Wild, O.: Nitrogen and sulfur deposition on regional and global scales: A multimodel evaluation, Global Biogeochem. Cycle, **20**, GB4003, https://doi.org/10.1029/2005GB002672, 2006.

Doney, S.C. The growing human footprint on coastal and open-ocean biogeochemistry, Science **328**, 1512-1516, DOI: 10.1126/science.1185198, 2010.

Dunlea, E.J. Herndon, S.C., Nelson, D.D., Volkamer, R.M., San Martini, F., Sheehy, P.M., Zahniser, M.S. Shorter, J. H., Wormhoudt, J. C., Lamb, B. K., Allwine, E. J., Gaffney, J. S., Marley, N. A., Grutter, M., Marquez, C., Blanco, S., Cardenas, B., Retama, A., Ramos Villegas, C. R., Kolb, C. E., Molina, L. T., and Molina, M. J.: Evaluation of nitrogen dioxide chemiluminescence monitors in a polluted urban environment, Atmos. Chem. Phys., 7, 2691–2704, https://doi.org/10.5194/acp-7-2691-2007, 2007.

Emerson, E.W., Hodshire, A.L., DeBolt, H.M., Bilsback, K.R., Pierce, J.R., McMeeking, G.R., and Farmer, D.K., Revisiting particle dry deposition and its role in radiative effect estimates, Proc. Natl. Acad. Sci. U.S.A., 117 (42), 26076-26082, doi: 10.1073/pnas.2014761117, 2020.

Finkelstein, P.L., Ellestad, T.G., Clarke, J.F., Meyers, T.P., Schwede, D.B., Hebert E.O. and Neal, J.A.: Ozone and sulfur dioxide dry deposition to forests: Observations and model evaluation, J. Geophys. Res., **105**, 15365-15377, https://doi.org/10.1029/2000JD900185, 2000.

Fowler, D., Pilegaard, K., Sutton, M.A., Ambus, P., Raivonen, M., Duyzer, J., Simpson, D., Fagerli, H., Fuzzi, S., Schjoerring, J.K., Granier, C., Neftel, A., Isaksen, I.S.A., Laj, P., Maione, M., Monks, P.S., Burkhardt, J., Daemmgen, U., Neirynck, J., Personne, E., Wichink-Kruit, R., Butterbach-Bahl, K., Flechard, C., Tuovinen, J.P., Coyle, M., Gerosa, G., Loubet, B., Altimir, N., Gruenhage, L., Ammann, C., Cieslik, S. Paoletti, E., Mikkelsen, T.N., Ro-Poulsen, H., Cellier, P., Cape, J.N., Horváth, L., Loreto, F., Niinemets, Ü., Palmer, P.I., Rinne, J., Misztal, P., Nemitz, E., Nilsoon, D., Pryor, S., Gallagher, M.W., Vesala, T., Skiba, U., Bruggemann, N. Zechmeister-Boltenstern, S., Williams, J., O'Dowd, Facchini, M.C., de Leeuw, G., Flossman, A., Chaumerliac, N. and Erisman, J.W.: Atmospheric composition change: ecosystems-atmosphere interactions, Atmos. Environ., **43**, https://doi.org/10.1016/j.atmosenv.2009.07.068, 5193-5267, 2009.

Fulgham, S.R., Millet, D.B., Alwe, H.D., Goldstein, A.H., Schobesberger, S., and Farmer, D.K., Surface wetness as an unexpected control on forest exchange of volatile organic acids, Geophys. Res. Lett., 47, e2020GL088745, https://doi.org/10.1029/2020GL088745, 2020.

Gordon, M., Li, S.-M., Stabler, R., Darlington, A., Hayden, K., O'Brien, J. and Wolde, M.: Determining air pollutant emission rates based on mass balance using airborne measurement data over the Alberta oil sands operations, Atmos. Meas. Tech., **8**, 3745-3765, https://doi.org/10.5194/amt-8-3745-2015, 2015.

Howarth, R.W. Review: coastal nitrogen pollution: a review of sources and trends globally and regionally, Harmful Algae, **8**, 14-20, https://doi.org/10.1016/j.hal.2008.08.015, 2008.

Jarvis, P.G. The interpretation of the variations in leaf water potential and stomatal conductance found in canopies in the field, Phil. Trans. R. Soc. Lond., B., **273**, 593-610, https://doi.org/10.1098/rstb.1976.0035, 1976.

Li, S.-M., Leithead, A., Moussa, S.G., Liggio, J., Moran, M.D., Wang, D., Hayden, K., Darlington, A., Gordon, M., Staebler, R., Makar, P.A., Stroud, C.A., McLaren, R., Liu, P.S.K., O'Brien, J., Mittermeier, R.L., Zhang, J., Marson, G., Cober, S.G., Wolde, M. and Wentzell, J.J.B.: Differences between measured and reported volatile organic compound emissions from oil sands facilities in Alberta, Canada, Proc. Natl. Acad. Sci., **114**, E3756-E3765, https://doi.org/10.1073/pnas.1617862114, 2017.

Liggio, J., Li, S.-M., Hayden, K., Taha, Y.M., Stroud, C., Darlington, A., Drollette, B.D., Gordon, M. Lee, P., Liu, P., Leithead, A., Moussa, S.G., Wang, D., O'Brien, J., Mittermeier, R.L., Brook, J.R., Lu, G., Staebler, R., Han, Yuemei, Tokarek, T.W., Osthoff, H.D., Makar, P.A., Zhang, J., Plata, D.L. and Gentner, D.R.: Oil sands operations as a large source of secondary organic aerosols, Nature, **534**, 91-94, https://doi.org/10.1038/nature17646, 2016.

Liggio, J., Li, S.-M., Staebler, R., Hayden, K., Darlington, A., Mittermeier, R.L., O'Brien, J., McLaren, R., Wolde, M. Worthy, D. and Vogel, F.: Measured Canadian oil sands CO2 emissions are higher than estimates made using internationally recommended methods, Nature Comm., **10**, 1863, https://doi.org/10.1038/s41467-019-09714-9, 2019.

Makar, P.A., Akingunola, A., Aherne, J., Cole, A.S., Aklilu, Y., Zhang, J., Wong, I., Hayden, K., Li, S.-M., Kirk, J., Scott, K., Moran, M.D., Robichaud, A., Cathcart, H., Baratzedah, P., Pabla, B., Cheung, P., Zheng, Q. and Jeffries, D.S.: Estimates of exceedances of critical loads for acidifying deposition in Alberta and Saskatchewan, Atmos. Chem. Phys., **18**, 9897-9927, https://doi.org/10.5194/acp-18-9897-2018, 2018.

Matsuda, K., Watanabe, I., Wingpud, V. and Theramongkol, P.: Deposition velocity of O_3 and SO_2 in the dry and wet season above a tropical forest in northern Thailand, Atmos. Environ., **40**, 7557-7564, https://doi.org/10.1016/j.atmosenv.2006.07.003, 2006.

Meyers, T.P., Hicks, B.B., Hosker Jr, R.P., Womack, J.D. and Satterfield, L.C.: Dry deposition inferential measurement techniques. II. Seasonal and annual deposition rates of sulfur and nitrate, Atmos. Environ., **25**, 2631-2370, https://doi.org/10.1016/0960-1686(91)90110-S, 1991.

Moran, M.D., Ménard, S., Pavlovic, R., Anselmo, D., Antonopoulos, S., Makar, P.A., Gong, W., Gravel, S., Stroud, C., Zhang, J., Zheng, Q., Robichaud, A., Landry, H., Beaulieu, P.-A., Gilbert, S., Chen, J. and Kallaur, A.: Recent advances in Canada's national operational AQ forecasting system. In: Steyn DG, Rao ST (Eds) Air Pollution Modelling and Its Application, Springer, Dordrecht, 289, https://www.researchgate.net/deref/http%3A%2F%2Fdx.doi.org%2F10.1007%2F978-94-007-5577-2_37, 2010.

Munger, J.W., Fan, S., Bakwin, P.S., Goulden, M.L., Goldstein, A.H., Colman, A.S. and Wolfsy, S.C.: Regional budgets for nitrogen oxides from continental sources: Variations of rates for oxidation and deposition with season and distance from source regions, J. Geophys. Res., **103**, 8355-8368, https://doi.org/10.1029/98JD00168, 1998.

Paulot, F., Malyshev, S., Nguyen, T., Crounse, J.D., Shevliakova, E. and Horowitz, L.W.: Representing sub-grid scale variations in nitrogen deposition associated with land use in a global Earth system model: implications for present and future nitrogen deposition fluxes over North America, Atmos. Chem. Phys. **18**, 17963-17978, https://doi.org/10.5194/acp-18-17963-2018, 2018.

Samset, B.H., Myhre, G., Herber, A., Kondo, Y., Li, S.-M., Moteki, N., Koike, M., Oshima, N., Schwarz, J.P., Balkanski, Y., Bauer, S.E., Bellouin, N., Berntsen, T.K., Bian, H., Chin, M., Diehl, T., Easter, R.C., Ghan, S.J., Iversen, T., Kirkevåg, A., Lamarque, J.-F., Lin, G., Liu, X., Penner, J.E., Schulz, M., Seland, Ø., Skeie, R.B., Stier, P., Takemura, T., Tsigaridis, K. and Zhang, K.: Modelled black carbon radiative forcing and atmospheric lifetime in AeroCom Phase II constrained by aircraft observations, Atmos. Chem. Phys. **14**, 12465–12477, doi:10.5194/acp-14-12465-2014, 2014.

Sickles, J.E. & Shadwick, D.S. Air quality and atmospheric deposition in the eastern US: 20 years of change. Atmos. Chem. Phys., **15**, 173-197, https://doi.org/10.5194/acp-15-173-2015, 2015.

Solomon, S., Quin, M., Manning, Z., Chen, M. Marquis, K.B., Averyt, M., Tignor, M., and Miller, H.L. (Eds): Climate Change 2007: The Physical Science Basis, IPCC *AR4*, Cambridge University Press, 2007.

Stull, R. Introduction to Boundary Layer Meteorology, Kluwer Academic Press, 1988.

Vet, R., Artz, R.S., Carou, S., Shaw, M., Ro, C.-U., Aas, W., Baker, A., Bowersox, V.C., Dentener, F., Galy-Lacaux, C., Hou, A., Pienaar, J., Gillett, R., Forti, M.C., Gromov, S., Hara, H., Khodzher, T., Mahowald, N.M., Nickovic, S., Rao, P.S.P. and Reid, N.W.: A global assessment of precipitation chemistry and deposition of sulfur, nitrogen, sea salt, base cations, organic acids, acidity and pH, and phosphorus, Atmos. Environ., **93**, 3-100, https://doi.org/10.1016/j.atmosenv.2013.10.060, 2014.

Wesley, M.L. Parameterization of surface resistances to gaseous dry deposition in regional-scale numerical models, Atmos. Environ., **23**, 1293-1304, https://ui.adsabs.harvard.edu/link_gateway/1989AtmEn..23.1293W/doi:10.1016/0004-6981(89)90153-4, 1989.

808 Wesley, M.L. & Hicks, B.B. A review of the current status of knowledge on dry deposition,
809   Atmos. Environ.*, **34,** 2261-2282,
810   https://ui.adsabs.harvard.edu/link_gateway/2000AtmEn..34.2261W/doi:10.1016/S1352-
811   2310(99)00467-7, 2000.

812

813 WHO, Ambient Air Pollution: A Global Assessment of Exposure and Burden of Disease, 2016.

814

815 Williams, E.J., Baumann, K., Roberts, J.M., Bertman, S.B., Norton, R.B., Fehsenfeld, F.C.,
816   Springston, S.R., Nennermacker, L.J., Newman, L., Olszyna, K., Meagher, J., Hartsell, B.,
817   Edgerton, E., Pearson, J.R., and Rodgers, M.O., Intercomparisons of ground-based NOy
818   measurement techniques, J. Geophys. Res., 103, 22,621-22,280,
819   https://doi.org/10.1029/98JD00074,1998.

820

821 Wright, L.P., Zhang, L., Cheng, I. and Aherne, J.: Impacts and effects indicators of atmospheric
822   deposition of major pollutants to various ecosystems - a review, Aerosol Air Quality Res., **18**,
823   1953-1992, https://doi.org/10.4209/aaqr.2018.03.0107, 2018.

824

825 Wu, Z., Schwede, D.B., Vet, R., Walker, J.T. Shaw, M. Staebler, R. and Zhang, L.: Evaluation
826   and intercomparison of five North American dry deposition algorithms at a mixed forest site,
827   J. Adv. Mod. Earth Sys., **10**, 1571-1586, https://doi.org/10.10292017MS001231, 2018.

828 Zhang, L., Moran, M.D., Makar, P., and Brook, J.R.: Modelling gaseous dry deposition in
829   AURAMS: a unified regional air-quality modelling system, Atmos. Environ., **36**, 537-560,
830   2002.Zhang, J., Moran, M.D., Zheng, Q., Makar, P.A., Baratzadeh, P., Marson, G., Liu, P.
831   and Li, S.-M.: Emissions preparation and analysis for multiscale air quality modeling over
832   the Athabasca Oil Sands Region of Alberta, Canada, Atmos. Chem. Phys., **18**, 10459-
833   10481, https://doi.org/10.5194/acp-18-10459-2018, 2018.

834

835 **Author Contribution:**

836 KH, SML, JL, SM, RM, RS, JO, MW all contributed to the collection of aircraft observations in the field.
837 KH, RM and JO made the SO_2, NO_y and pSO_4 measurements and carried out subsequent QA/QC of data.
838 RM analyzed canister VOCs and provided OH concentration estimates. SM provided OH estimates from
839 MCM modelling as a comparison. AD contributed to the development of TERRA. JL wrote the Monte
840 Carlo code. PM and AA ran the model and provided model analyses. JZ provided emissions data. LZ and
841 RS provided deposition algorithm parameters. KH and SML wrote the paper input from all co-authors.

842 **Code availability**

843 All the computer code associated with the TERRA algorithm, including for the kriging of pollutant data, a
844 demonstration dataset and associated documentation is freely available upon request. The authors request
845 that future publications which make use of the TERRA algorithm cite this paper, Gordon et al., Liggio et
846 al., or Li et al. as appropriate.

847 **Data availability**

848 All data used in this publication are freely available on the Canada-Alberta Oil Sands Environmental
849 Monitoring Information Portal: https://www.canada.ca/en/environment-climate-change/services/oil-
850 sands-monitoring/monitoring-air-quality-alberta-oil-sands.html
851

852 **Acknowledgements:**